Dislocation structures and their relationship to strength in deformed nickel microcrystals

D.M. Norfleet [a,*], D.M. Dimiduk [b], S.J. Polasik [a], M.D. Uchic [b], M.J. Mills [a]

[a] *Department of Materials Science and Engineering, The Ohio State University, 477 Watts Hall, 2041 College Road, Columbus, OH 43210, USA*
[b] *Air Force Research Laboratory, Materials and Manufacturing Directorate, AFRL/RXLM Bldg. 655, 2230 Tenth Street, Wright Patterson, AFB, OH 45433-7817, USA*

Abstract

The present work uses focused ion beam methods to prepare samples for transmission electron microscopy in order to quantitatively characterize changes in the dislocation substructures obtained from undeformed and deformed pure Ni microcrystals having sample diameters that range from 1 to 20 μm. Following deformation, the dislocation density measured in the microcrystals is on average in excess of their expected initial density, with an apparent trend that the average density increases with decreasing microcrystal size. These dislocation density data are used to assess the contributions of forest hardening to the flow strength of the microcrystals. The combined effects of lattice friction, source-truncation hardening and forest hardening are found to be insufficient to fully account for the large flow strengths in smaller microcrystals.
© 2008 Acta Materialia Inc. Published by Elsevier Ltd. All rights reserved.

Keywords: Nickel; Dislocation density; Plastic deformation; Size effects; TEM

1. Introduction

Quantitative and predictive techniques for representing the mechanical behavior of metals are limited by an under-developed understanding of length or size-scale effects on deformation. However, recent advances in microsample fabrication methods enable new capabilities to investigate mechanical size effects associated with sample dimensions at the micro- and nano-scale. For example, micro-sized compression samples have been fabricated from bulk single crystals using focused ion beam (FIB) microscopes [1–4]. Unlike early whisker experiments, at least some of these microcrystals contain microstructures that are nominally representative of bulk crystals with a grown-in dislocation forest [1]. Still, the results of experimental tests indicate a dramatic increase in strength as the sample dimensions are reduced to sizes less than ∼20 μm in diameter [1–12].

Although much experimental data has been acquired with regard to the strength of microcrystals, only very recently have insights begun to emerge pertaining to the multiple dislocation micromechanisms that may be driving this behavior. This in turn has led to several hypotheses based on intuitive insights, classical theory and dislocation plasticity models. Greer and Nix [2,7] suggested that strengthening of small crystals is associated with the "starvation" of mobile dislocations, as the proximity of free surfaces allows for the movement of dislocations out of the sample before they have a chance to multiply. Similarly, Deshpande et al. [13,14], using two-dimensional (2D), discrete dislocation plasticity simulations mimicked selected ideas proposed by Greer and Nix, whereby the rate of dislocations exiting the sample exceeded the dislocation nucleation rate at prescribed sources. The simulations used a narrow stress range for source activation, and thus the simulated flow stresses reflected the total number of dislocations present which scaled with sample size within the 2D simulations. Arguments similar to those posed from

* Corresponding author.
 E-mail address: dmnorfleet@esi-il.com (D.M. Norfleet).

simulations were used by Volkert and Lilleodden [4] to suggest that free-surface image stresses and source-limited behavior lead to a loss of mobile dislocation density in their experimental tests, resulting in an increase in stress to activate dislocation sources as the sample size decreased. Most recently, an in situ transmission electron microscopy (TEM) deformation study by Shan et al. [11] showed that a ~150 nm diameter Ni microcrystal appears to be dislocation free before and after deformation; however, the same study showed that a nearly 300 nm diameter Ni microcrystal contained dislocations even after sustaining a load of ~2.6 GPa.

Alternatively, considering selected statistics of dislocation source lengths and 3D dislocation simulations, Parthasarathy et al. [15] proposed a strengthening mechanism due to the formation of single-arm sources, as small sample dimensions infringe upon the dimensions required for conventional sources to multiply [16,17]. Still other studies provided evidence for an excess dislocation density being present for FIB-prepared undeformed samples and deformed samples when the height-to-diameter ratios are small or when sub-grain boundaries are present [8–10]. Those studies conclude that strain gradients lead to the observed slip response [9]. Finally, following the ideas of Sevillano et al. [18], Dimiduk et al. [1] found experimental consistency for strengthening by a statistical alteration of the mean-field forest that results from limiting the single-crystal dimensions.

Thus, the present investigation seeks to refine these prior results and hypotheses from direct observations of the dislocation structures found in Ni microcrystals. This study quantitatively characterized changes to the dislocation substructure for deformed Ni microcrystal samples previously described in other publications [1,3,19]. Specifically, dislocation-density measurements were made on undeformed bulk and microcrystal samples and deformed samples ranging from 1 to 20 μm in diameter. These results are discussed within the context of the current notions regarding microcrystal deformation.

2. Experimental procedures

2.1. Microcrystal preparation and testing

Nickel microcrystal compression samples were fabricated using a FIB (FEI model DB235), following the procedures published elsewhere [1,20]. The samples varied from 1 to 40 μm in diameter, with their loading axis aligned along the [269] single-slip direction. These samples were subsequently compressed uniaxially, using an MTS Nano-Indenter XP fitted with a flattened diamond tip. Nominal deformation strain rates of $10^{-4}\,\mathrm{s}^{-1}$ were achieved under a hybrid loading method, where a programmed constant-displacement rate was imposed on the sample. If under the closed-loop control the sample displacement was found to exceed the programmed value, the control loop forced a constant load hold. That is, the sample was permitted to

experience either an increasing load or a load hold, but never load shedding until the test was complete. As noted in other work, the nanoindentor permits lateral deflection of the loading platen [1]. Consequently, even microcrystals oriented for single slip will deform in the absence of significant kinematical constraint within their central region, provided that the height-to-diameter ratios (in this case ~2.5:1) provide for slip planes that intersect free surfaces rather than the compression platens or "dead zones" known to occur during compression testing [21–23].

2.2. TEM sample preparation method

The majority of the foils examined in this study were prepared from slip bands in the microcrystals. For these samples, the primary slip traces are clearly visible after deformation (Fig. 1). The slip traces were used to align the samples for subsequent TEM sample extraction along the primary active $(\bar{1}11)$ slip plane. Owing to the small size of these samples, conventional TEM sample preparation techniques were not feasible and, therefore, FIB fabrication methods were used to make the TEM foils [24]. This particular study used an FEI Strata DB 235 and an in situ micromanipulator (OmniProbe™) to extract and subsequently thin the samples to electron transparency.

To ensure that the TEM foil contained a slip trace, a two-step procedure was used to define the plane of the slip trace. The first step consisted of depositing fiducial markers of platinum that were placed at multiple locations along a particular slip trace. Here, the fiducial markers were in the shape of a cross, where the intersection of the cross and the surface trace of the slip plane coincided, as shown in Fig. 1. The second step consisted of covering the entire slip-plane region with a carbon film to protect the sample during FIB thinning. During the thinning process, the Pt crosses initially appear on the cross-sectional surface as two distinct points along the outer edge of the microsample. As this cross-sectional surface is milled closer to the active slip plane, these two points move closer together and ultimately merge into a single point at the position of the slip trace.

After thinning the foil to thicknesses that were marginally electron-transparent with the DB 235, a second milling procedure was employed both to reduce the surface ion-damage layer produced by the 30 kV Ga$^+$ ions and to thin the foil further for improved imaging. A Gatan Duo Mill was used to perform low-energy milling at voltage settings of 1–2 kV, a beam current of 0.5 mA, and a milling angle of 13°. Milling times varied between 30 min and a few hours in order to produce optimal samples.

Upon examination of the TEM samples, it was determined that bending in the foils made conventional diffraction-contrast imaging problematic, especially over entire pillar sections. Therefore, bright-field scanning TEM (BF-STEM) imaging was used to minimize these effects [25,26]. Maher and Joy [26] have shown that, by increasing the convergence angle in STEM, the signal-to-noise
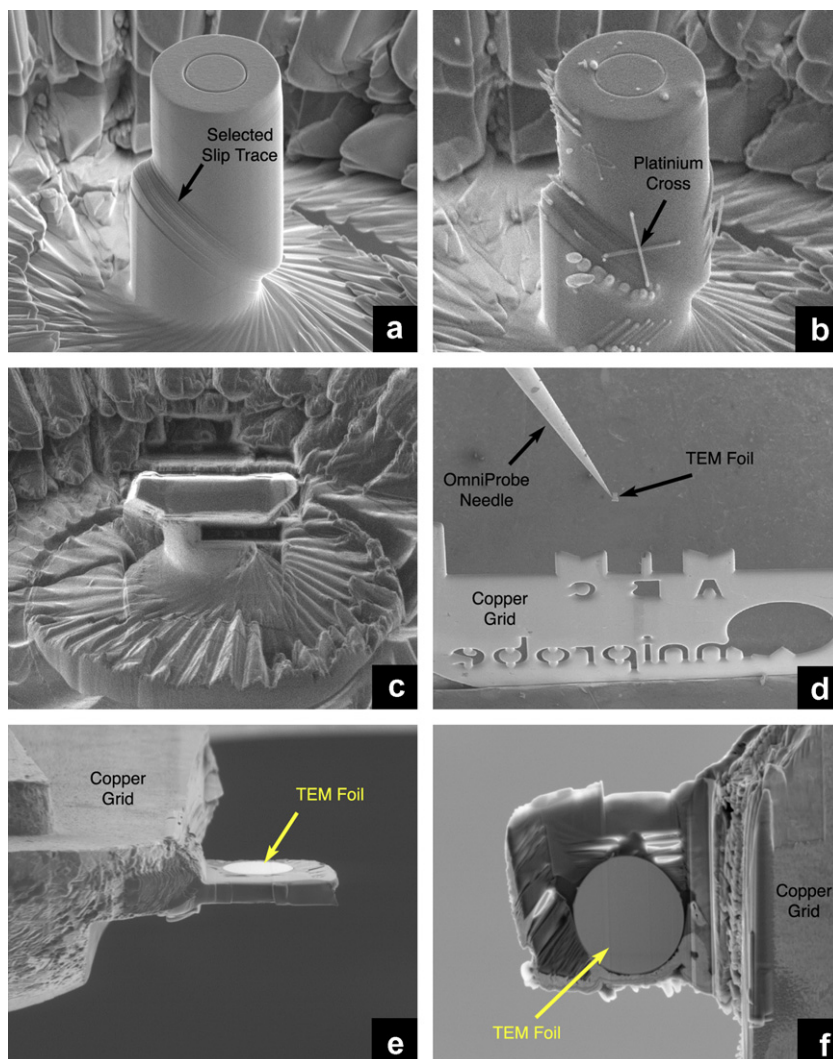
Fig. 1. A series of secondary electron images taken from the FIB to illustrate the TEM extraction procedure from a 5 μm diameter sample. (a) Typical sample after deformation indicating several slip traces; (b) platinum crosses are placed along regions of the desired slip trace to act as fiducial marks during the final thinning process; (c) excess material is FIB-milled away to leave only the slip trace of interest; (d) the TEM sample is attached to the OmniProbe™ needle and then transferred to a copper grid; (e) the TEM foil is attached to the copper grid using carbon and platinum deposition; (f) the TEM foil is thinned to electron transparency from both sides until the platinum fiducial marks are reached.

ratio is increased, enabling examination of thicker samples and minimizing contrast due to thickness fringes and bending contours. However, the increase in convergence angle also causes a loss in dynamical information, such as contrast related to dislocations and stacking faults. Therefore, a convergence angle of 9 mrad was used as a compromise between minimizing the contrast of the bending contours while maintaining adequate contrast from the dislocations. Maher and Joy also demonstrated that, when an appropriate convergence angle is used, a two-beam condition can be obtained, and "g·b analysis" can be performed to determine dislocation Burgers vectors. All TEM microscopy for this study was performed on a 200 kV FEI/Phillips Tecnai TF20 fitted with a field-emission electron source. Energy filtering and image collection was carried out using a Gatan imaging filter (GIF) and BF/DF STEM detector.

2.3. Dislocation density measurement

Dislocation densities were calculated using two different methods. A line-intercept method was used for the TEM foils sectioned parallel to the slip planes, whereby five randomly placed lines of different angular orientation are drawn over the TEM images. This was facilitated using Fovea Pro 4.0 image-processing and measurement software from Reindeer Graphics. Points are manually placed at the intersection of each dislocation image with the random lines. This procedure is shown in Fig. 2 for a deformed 10 μm microcrystal. The dislocation density ρ is simply the number of points N divided by the total line length of the random lines L_r, multiplied by foil thickness t [27]:
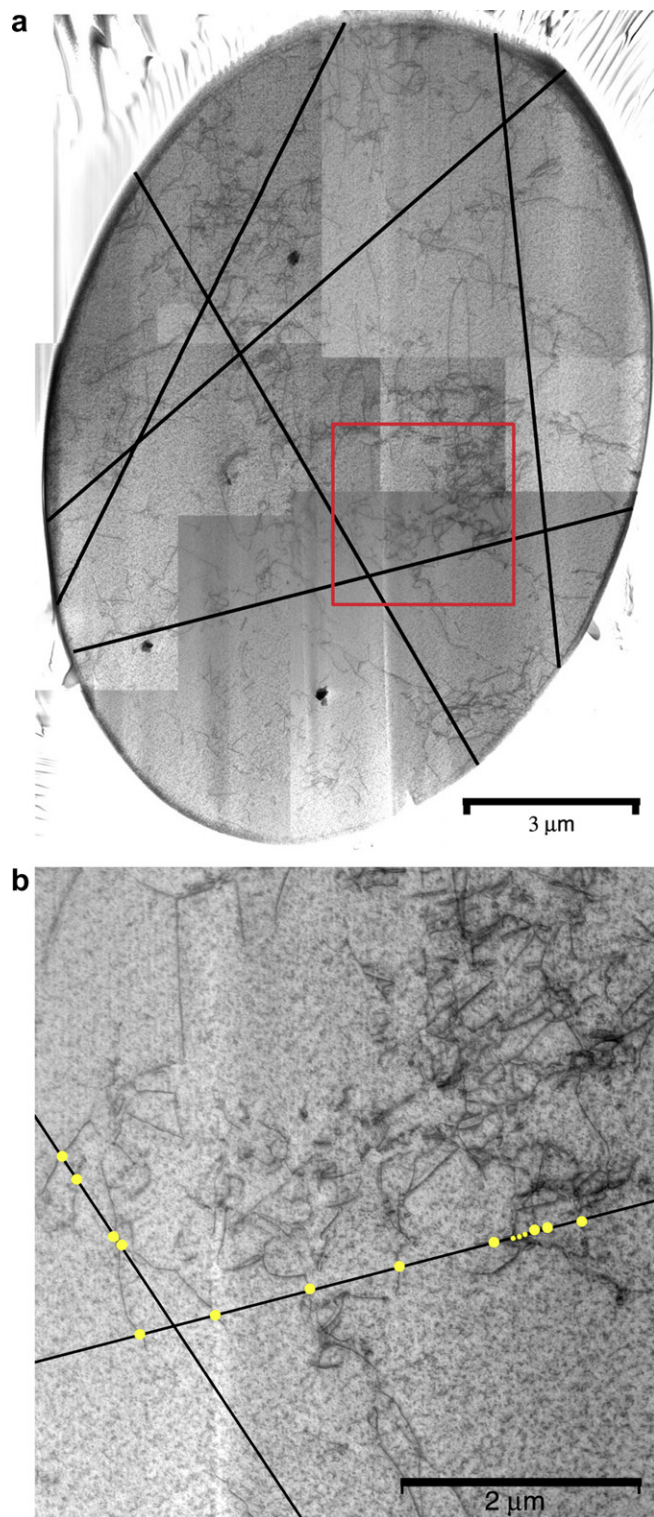
$$\rho = \frac{N}{L_r t} \tag{1}$$

Fig. 2. Example of one of the procedures used for dislocation density measurements, the line-intercept method: (a) random lines are superimposed a BF-STEM image taken from a deformed 10 μm diameter microsample; (b) marks are placed at each point where a dislocation intersects a line.

The accuracy of the density measurements determined using this formula relies foremost upon precise measurement of the foil thickness which, in the present study,

was determined using an energy-filtered convergent-beam electron-diffraction (EF-CBED) technique [28,29], and comparison of intensity oscillations (i.e. Kossel–Möllenstedt fringes) in the $\{000\}$ and $\{hkl\}$ disks with simulations using "JEMS" software [30,31]. Energy filtering was employed to accentuate the fringe patterns by eliminating inelastically scattered electrons using an energy window of ± 10 eV centered about the 200 keV elastic-energy peak. Kelly et al. [29] have shown that thickness measurements with an accuracy of $\pm 2\%$ or better are routinely determined using this type of CBED measurement.

A second technique was used to check the reliability of the dislocation-density results obtained from the line-intercept method. In this method, the density was measured by manually tracing and measuring the total dislocation line length L_t within select TEM foils using Fovea Pro software, which is a much more tedious task to perform compared with the line-intercept method. The total dislocation density ρ_t was calculated using the following relationship [32]:

$$\rho_t = \frac{L_t}{At} \tag{2}$$

where A is the imaged foil area. The difference in the measured densities using these two techniques was found to be minimal compared with other errors that are present during the measurement (see Section 2.4). For instance, measurements performed on the same region of the 10 μm sample shown in Fig. 2 by the tracing method produced a dislocation density of 6.49×10^{12} m^{-2}, while the line-intercept method produced a density value of 7.11×10^{12} m^{-2} (a 9.5% error in this case). For this reason, the line-intercept method was determined to be sufficient for dislocation-density measurements. For the measurements taken from foils cut parallel to slip planes, all imaged dislocation segments were considered, which resulted in a measured total dislocation density for the sample (as opposed to the forest-dislocation density).

Note that the "relaxed" diffraction conditions caused by the converged beam under BF-STEM enables simultaneous imaging of all dislocations present within the TEM foil, providing a total dislocation density measurement. It is only when very precise diffraction conditions are applied (see Section 3.4) that invisibility conditions are achieved using BF-STEM.

2.4. Errors and uncertainty associated with dislocation density measurements

There are several possible sources of error and uncertainty related to the present TEM-based dislocation density measurements. One common source of error was mentioned earlier and is associated with measuring the foil thickness, $\pm 2\%$ being typical for CBED measurements. However, this value assumes a constant foil thickness over the viewing area, which is not the case for real samples. During the FIB-thinning of the extracted TEM foils, there

is usually a taper to the samples from one end to the other, which is evident in thickness measurements taken at different locations within a foil. Fig. 3 shows a plot of three thickness measurements taken along the long axis of the elliptical-shaped view areas of the foils, for both a 2 and a 20 μm diameter microcrystal. This plot demonstrates that, for the preparation methods used in this study, the taper is constant and, therefore, one must only measure the thickness in the middle of the foil to make a reasonable determination of thickness. The error associated with a single thickness measurement was determined using a linear fit between the "top" and "middle" data points in Fig. 3, and extrapolating this line to the "bottom" data point. Given that the distances between the "top", "middle" and "bottom" are ∼10 μm for the 20 μm samples, and comparing the extrapolated value to the measured value, an additional error of 3% was determined. From the analysis of these two foils, it was determined that using only a single measurement increases the error of the thickness value from ±2% to ±5%. Thus, for most of the foils, only a single measurement from the center of the foil was used to determine the thickness.

A second source of error is related to the difficulty in imaging dislocations that are grouped closely together, whereby their intensity profiles overlap under bright-field-imaging conditions. The error associated with this overlap was determined by measuring N, the number of line-intersections, for a given viewing area under both bright-field and dark-field imaging conditions. The latter condition produces images of dislocations that are narrower, enabling even closely spaced dislocations in bundles to be discriminated, but with a much more limited field of view due to obscuring bend contours. Dislocation density measurements on the same sample regions obtained with both imaging modes indicate a ∼30% underestimation in N when using BF-STEM. This error and that due to sample thickness variation are combined in quadrature, and the results are displayed using error bars for the density measurements that are shown in the rest of this study.

Another error is simply related to the geometry of the TEM foil and the dislocations that lie parallel to the foil normal. These dislocation segments are then truncated to roughly the thickness of the TEM foil. As a result, and considering tilting limitations in the microscope, imaging such dislocation segments is difficult, and they may not be fully counted in the total density measurements. As such, all dislocation values reported here should be considered as a lower bound. Naturally, the errors discussed here are associated with the measurements made for each TEM sample. Any uncertainties associated with the representative nature of the dislocation structure in any given slip trace relative to the overall sample response or the accuracy with which the samples were consistently extracted from slip traces exist over and above the actual measurement errors. Selected aspects of these uncertainties are discussed later.

3. Results

3.1. Microsample compression testing

The results of compression testing indicate a dramatic increase in flow strength as the sample size is decreased [1]. Fig. 4 is a composite plot showing engineering flow stress vs. engineering strain for all sample sizes that were tested. More complete test results have been reported elsewhere [1,6]. Evident from the flow curves is a distinct transition in strain-hardening behavior at sample sizes of 10 μm or less. For samples >10 μm a strain-hardening rate (SHR) ∼G/2000 (where G is the shear modulus) is observed, as is typical of Stage I glide. However, for samples <10 μm, there is a variable, sometimes broad, yielding transition that includes intermittent burst periods of flow under conditions of no strain hardening. These burst-like events have been linked to the same scale-free behavior observed in selected macroscopic systems, such as plate tectonics of
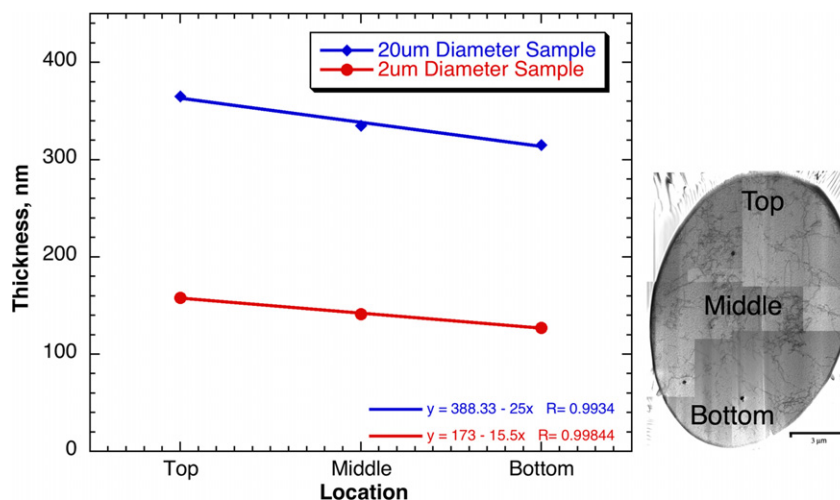

Fig. 3. Thickness variation across a 2 and a 20 μm slip-plane foil. The variation is caused during the final thinning process of the TEM foil.

a Pure Ni Microcrystal Data <269> Orientation
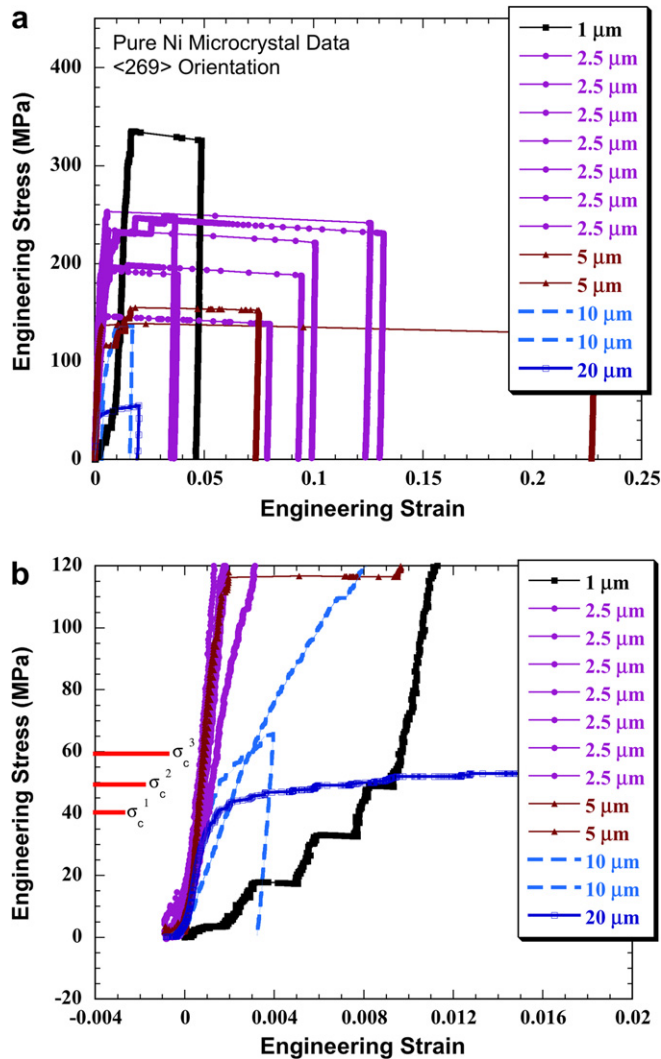

b

Fig. 4. (a) Nickel microcrystal compression results. (b) Critical stresses needed to activate each of the three primary slip systems, calculated from the Schmid factors based on the [269] loading direction.

the earth [19,33–35]. As recently articulated by Csikor et al. [33], such intermittency is natural and manifestly present in the flow response of small crystals.

3.2. Dislocations in undeformed crystal regions

In order to establish a reference for interpreting the microcrystal deformation behavior, assessments were made of the pre-existing dislocation structure ρ_o within the macroscopic crystal from which the microcrystals have been machined. To this end, TEM samples were extracted from fully machined but untested microcrystals using sectioning planes oriented parallel to the same primary $(\bar{1}11)$ plane as examined for the deformed samples. A low-magnification view of the undeformed regions can be seen in Fig. 5. From this image and others, values of ρ_o were determined to be $\sim 1.4 \times 10^{13}$ m^{-2}. The large values for ρ_o clearly distinguish the initial state of the pure Ni microcrystals studied here and in Refs. [1,3] from that of the near-dislocation-free
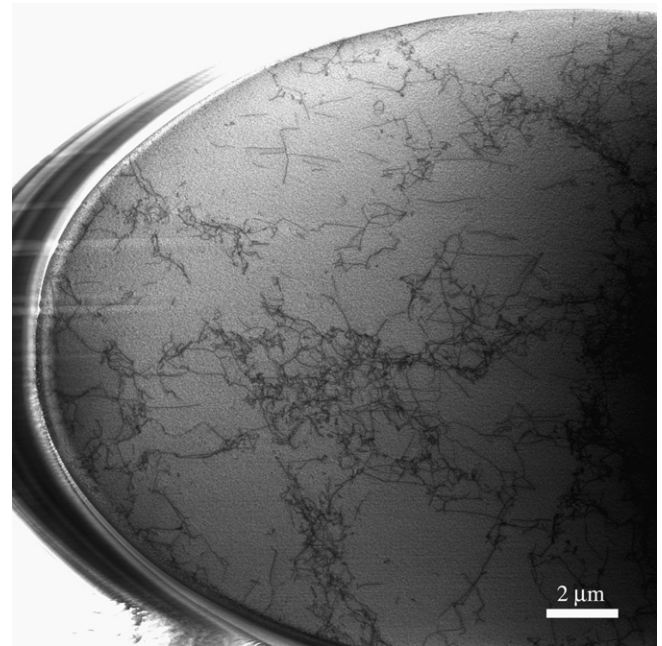

Fig. 5. BF-STEM image taken from an undeformed microcrystal along the same $(\bar{1}11)$ plane that is active in the deformed samples. This image illustrates the large initial dislocation density that is present prior to loading.

state reported previously for metallic whiskers [36]. Also obvious from Fig. 5 is that microcrystals machined from the bulk could contain a widely varying initial average dislocation density, consistent with the 3D spatial statistics that may be inferred from Fig. 5.

In addition to the $(\bar{1}11)$ foils, TEM samples were also extracted at 45° to the loading direction, having no specific foil normal. As a result of selecting such foil orientations, the observed structures and measured dislocation densities should correspond to the forest-dislocation density ρ_f that will be encountered by the glide system(s) of deformation. Such is not the case for foils sectioned parallel to the primary glide plane and, for those measurements, some correction factor must be used to determine ρ_f, as discussed later. Density measurements from these off-parallel foils ranged from $\rho_o = \rho_t = \rho_f = 5.5 \times 10^{12}$ m^{-2} to 1.6×10^{13} m^{-2}. Note that these values are consistent with a prior study [37].

3.3. Dislocation structure vs. sample size

Examination of the slip-plane cut foils from 1, 2, 5, 10 and 20 μm microcrystals demonstrates that a deformation structure is evident in all the foils, as shown in Fig. 6. Magnified views of foils from two 2 μm pillars and one 1 μm pillar are shown in Fig. 7. In each case, the dislocation structure resembles that of Stage I glide and contains a dense population of predominately near-edge-character dislocation tangles [38]. The presence of multipole configurations in these tangles has been established by changes to apparent dislocation positions when using $\pm g$-vector
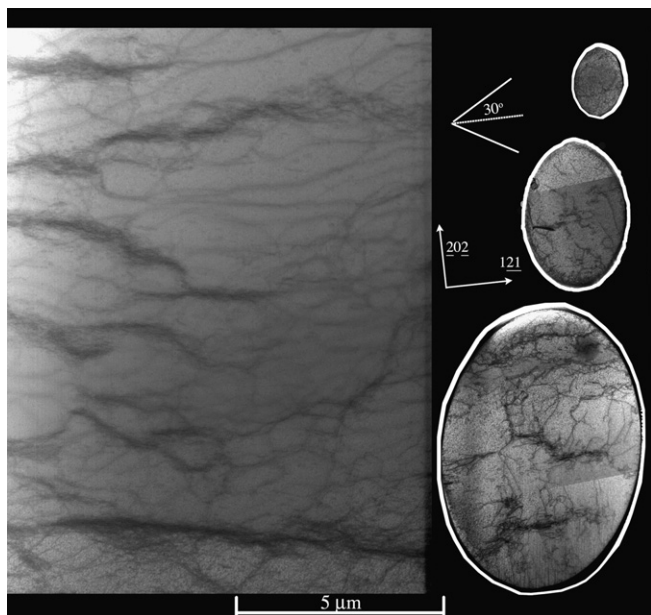
Fig. 6. BF-STEM images taken along the $(\bar{1}11)$ slip-plane from 1 2, 5 and 20 μm diameter nickel microcrystal samples following deformation. Directions deviated by ±30° from the pure edge line orientation for the primary slip system are indicted.
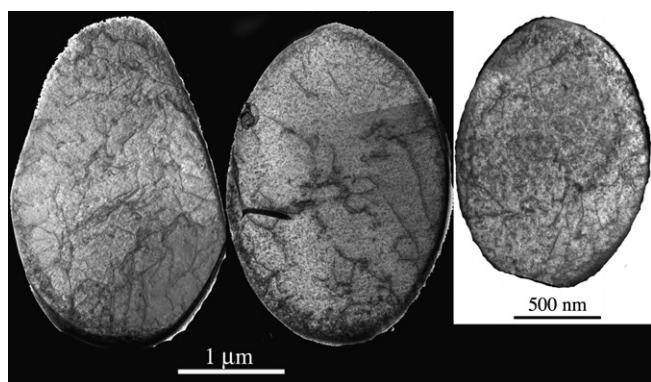

Fig. 7. Magnified views taken from three microcrystals, two 2 micron and one 1 micron.

diffraction conditions. These dislocation tangles consist of multipolar dislocation braids that are believed to be formed following annihilation of screw-character segments by cross slip [39].

Mader et al. [38] found that dislocations in deformed bulk-crystal Ni lie predominately in directions within the glide plane, making angles of 30° or less with the pure-edge line directions. Inspection of Fig. 6 illustrates that, for the sizes studied, there is a similar, preferred orientation of the dislocation tangles. Figs. 6 and 7 also indicate that the scale of the inter-braid spacing within the slip planes remains nominally constant as the sample dimensions are decreased. The inter-braid spacing was measured to be ∼2.2 μm for the 20 μm diameter microsamples [37,40]. This spacing agrees well with the estimated strong-obstacle spacing based on a random array of dislocation obstacles

[18,41]. If an average starting dislocation density ρ_o of 5×10^{12} m^{-2} is assumed for the material, only half these dislocations contribute to the forest [42] and, of the forest dislocations, ∼20% form junctions strong enough to arrest dislocation motion [43–45]. Thus, the strong-obstacle spacing is given by $1/\sqrt{\frac{\rho_o}{10}}$ or ∼1.4 μm. Mader et al. [38] measured an inter-braid spacing of 10 μm in Ni, although the initial dislocation density was $\rho_o = 10^{11}$ m^{-2}, resulting in a larger inter-braid spacing than that found in the present study.

3.4. Evidence for multiple slip

Owing to the large stresses experienced by the microsamples, it is expected that multiple slip systems may be operative based upon the measured bulk-crystal flow stress. Schmid factor calculations indicate that, with a loading direction of [269], the three slip systems with the highest resolved shear stress are:

(1) $1/2[10\bar{1}](\bar{1}11)$, Schmid factor $= 0.48$.
(2) $1/2[10\bar{1}](111)$, Schmid factor $= 0.40$.
(3) $1/2[110](\bar{1}11)$, Schmid factor $= 0.35$

Using the bulk-crystal flow stress, the critical stresses required to activate each of these slip systems $\sigma_c^1, \sigma_c^2, \sigma_c^3$ are calculated and illustrated on the stress–strain curves presented in Fig. 4b. These results suggest that, for samples <20 μm in diameter, multiple slip systems should be active.

In fact, slip-trace analysis of the microsamples after loading indicates that $(\bar{1}11)$ is the primary active slip plane for all samples tested; however, for samples <10 μm in diameter, a secondary system on the (111) plane is operative as well [1,37]. From the size and direction of the slip steps, the majority of the strain is accrued along the primary $(\bar{1}11)$ system at all sizes tested, but a secondary slip system (111) becomes more frequent (as evidenced by new non-primary slip planes) at smaller sizes [1].

TEM observations also indicate the presence of all three active slip systems in several of the slip-plane cut foils, whereby $\mathbf{g} \cdot \mathbf{b}$ analysis was performed, and the results are shown in Fig. 8. The numbers on these images correlate with the slip system, as determined from this analysis, for each dislocation segment 1, 2 or 3 designated above (note that, for reasons of clarity, not all dislocation segments have been labeled). These TEM results indicate that the majority of dislocations are $1/2[10\bar{1}]$ $(\bar{1}11)$, type with roughly equal contributions from the other two systems. Although each of these slip systems experiences a different resolved shear stress, as illustrated in Fig. 4b, the stresses reached in these microsamples are large enough to activate all three slip systems, at least on the local scale.

3.5. Measured dislocation density vs. sample diameter

The slip-trace dislocation densities for several deformed microsamples were measured using the line-intercept
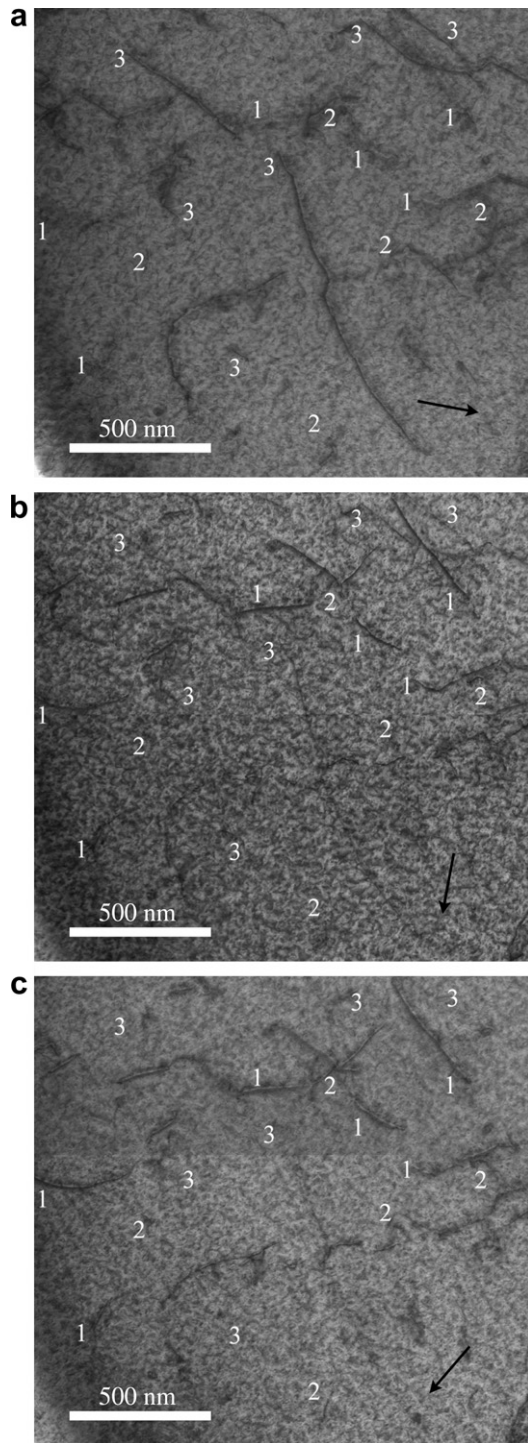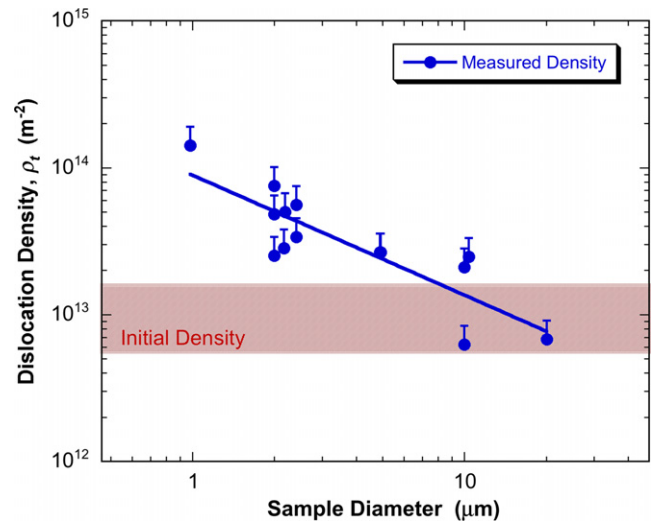
Fig. 9. Dislocation density measurements performed using the line-intercept method indicating an increase in the dislocation density as microsample dimensions are reduced.

situ or postmortem TEM experiment, the dislocation structure observed is representative of that stored from the very end of the loading cycle. Careful attention was paid such that the samples were not unloaded until flow had ceased from a strain-burst event, i.e. until the natural strain-hardening processes led to a cessation of deformation. Therefore, one is assured that the observed dislocation substructure was able to sustain the final stress prior to unloading, as was the remaining volume of material outside the selected slip traces. It is this final shear stress and ending dislocation structure that was used in all experimental measurements and calculations, unless otherwise stated.

In spite of the increase in dislocation density with decreasing sample size, there appears to be no evidence that the observed dislocation density is a significant function of the imposed total strain level, as revealed by the data
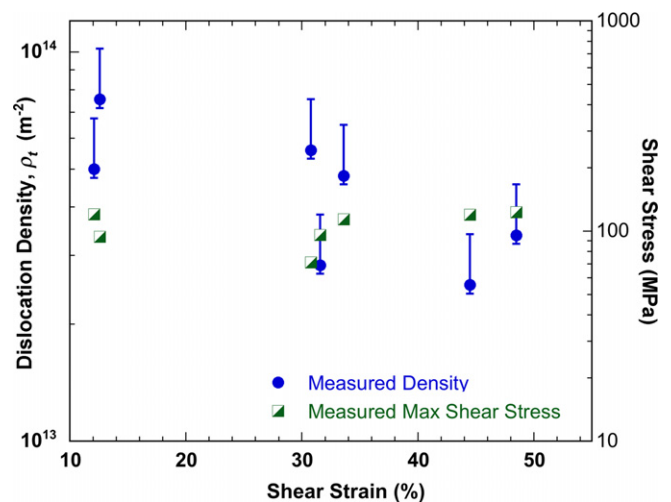

Fig. 8. Invisibility conditions from a 2 μm microcrystal for the three highest resolved shear stressed slip systems, designated 1, 2 and 3, respectively. (a) $g = (\bar{1}\bar{3}1)$, the invisibility condition for slip system 1; (b) $g = (\bar{2}0\bar{2})$, the invisibility condition for slip system 2; (c) $g = (\bar{1}1\bar{3})$, the invisibility condition for slip system 3.

Fig. 10. Density measurements from 2 μm diameter nickel samples as a function of nominal strain and maximum shear stress.

method described previously. These data are plotted on a log–log plot and shown in Fig. 9. The most important result from these measurements is the on-average increase in the dislocation content (relative to the average bulk-crystal content) as the sample size is decreased. As with any ex

shown in Fig. 10 for 2 μm diameter samples. In fact, large measured densities exist on slip traces after only 11% shear strain. These structures are not substantially changed at higher strains (consistent with the Stage I glide model [39]). The results suggest that dislocation substructure is forming and sustaining the large observed stresses very early in the loading cycle. Perhaps the structures are formed during the early strain hardening, or exhaustion-hardening interval [1,17], but this point requires further investigation. This result is supported by the shapes of the flow curves for 2 μm diameter samples in Fig. 4 which exhibit little to no strain hardening after reaching the flow stress. The result is also consistent with the patterning of the dislocation substructure that is indicative of Stage I glide. Thus, dramatic increases in density are not to be expected with large changes in strain beyond the initial exhaustion-hardening regime.

3.6. Dislocation structure in deformed macroscopic crystals

In addition to examining the average starting dislocation density in selected microcrystals, TEM foils were prepared from deformed bulk single-crystal compression samples using conventional sectioning and electropolishing methods. The foils were oriented parallel to the primary $(\bar{1}11)$ slip-plane traces for those crystals. A BF-TEM image of a deformed bulk $(4 \times 4 \times 10 \text{ mm})$ compression sample is shown in Fig. 11, along with a BF-STEM image from a deformed 2 μm diameter microcrystal, where both samples experienced the same nominal engineering strain of ~2%. Qualitatively, the dislocation ensembles and heter-
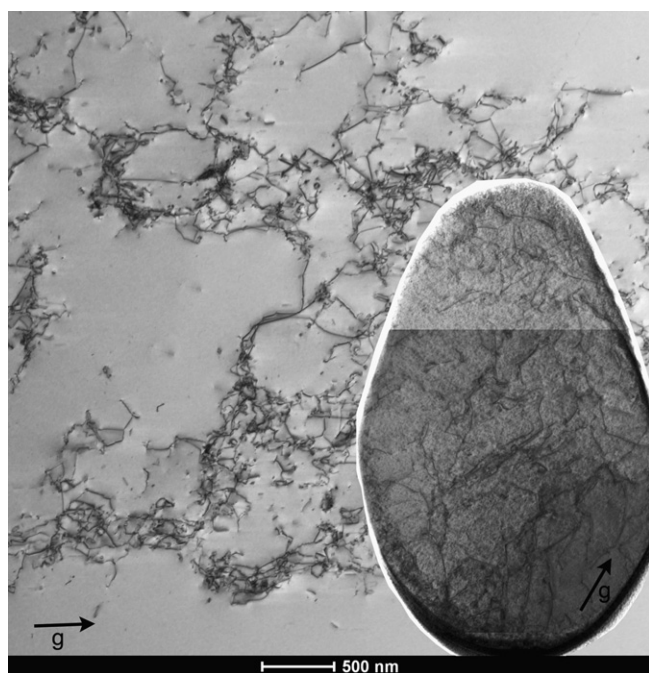

Fig. 11. BF-STEM image taken from a bulk compression sample and a 2 μm diameter microcrystal. The nominal strain levels are within 1% of each other.

ogeneity are similar between the two samples. The bulk sample exhibits larger regions that contain little or no dislocation content; however, it is also possible that the microcrystals, by chance, could have been fabricated from a high-density region. For any systematic conclusions to be drawn from these defect-free zones, more TEM samples are needed from small (~2 μm) microcrystals containing similar strains, both within and external to slip traces. Nevertheless, Fig. 9 indicates that, after deformation and examination of seven 2 μm samples, one consistently finds a higher average slip-trace dislocation density than that observed at larger sizes, or after deformation of bulk crystals.

4. Discussion

4.1. General aspect of deformed substructures

The presence of near-edge character multi-polar braid structures, as seen at various size scales in Fig. 6, implies that co-planar slip as well as localized cross slip occurs during plastic deformation, as expected. Note that the inter-planar screw-character dipole annihilation distance h_s may be expressed as [41]

$$h_s = \frac{Gb \sin\beta}{2\pi(\tau_o - s\tau_f)} \tag{3}$$

where b is the magnitude of Burgers vector, β is the angle between the glide and cross-slip planes (54.7°), τ_o is the frictional stress, s is the ratio of Schmid factors on the cross-slip and primary planes, and τ_f is the current flow stress. Using values appropriate for Ni, h_s takes on values of ~0.5 μm and larger. Thus, for pure Ni, screw-character dislocations are expected to have extremely short lifetimes within the crystals because of cross-slip annihilation. The result of such ready annihilation is likely to be an extensive jog-segment forest connected with near-edge-character intra-planar dislocation debris and inter-planar multipole bundles. Such a jog-segment forest may contribute dislocation sources on non-primary slip systems that are also highly stressed in microcrystals.

There is no consistent evidence for dislocation pile-ups or dislocation-free zones near the free surfaces of the microcrystals. The presence of such features would be an indication that the Ga^+ ion damage has created a hardened case on the sample's surface, or that image forces deplete the sample of dislocations, as some have suggested. The Ga^+ ions clearly do produce localized, near-surface defects, as is evident in the "speckled" contrast seen in the TEM foils produced by the FIB operation. However, Shan et al. [11] has shown, using in situ TEM deformation experiments on sub-micron Ni pillars, that this initial damage layer "mechanically anneals" at the free surfaces during deformation. The observations provide support for the contention that the Ga^+ ion damage is not a dominant factor dictating the strength of Ni microcrystals, although other materials may behave differently.

4.2. Variation in dislocation density with sample size

The apparent increase in average slip-trace dislocation density with decreasing sample size seen in Fig. 9 may be attributed to several possibilities. The first is related to the activation of the secondary slip systems. As indicated by the SEM studies performed by Dimiduk et al. [1], secondary-slip activity becomes more apparent at smaller sizes. These increase the forest density and are expected to increase the effective storage rate of the primary system, creating an increase in total density as sample sizes are reduced. The measurements may also be affected by slip localization at smaller sizes. For the larger samples, slip may occur on many possible planes along the gage length of the sample. However, as the sample dimensions are reduced and, because of the expected weakest-link statistical process of slip, the number of possible low-stress slip planes decreases with sample size (statistical occurrences are altered). This creates a higher probability of localized slip on a given slip trace, perhaps resulting in a larger slip-trace dislocation density at smaller sizes.

The trend seen Fig. 9, in conjunction with the measurements of significant initial dislocation content, contradicts the hypothesis that the increase in strength of microcrystals can be solely attributed to dislocations leaving the microcrystal (one type of starvation mechanism) [7,11]. Apparently, samples may also be mobile-density "starved" because of relatively effective dislocation pinning and a reduced number of weak-link dislocation sources. In the original starvation scenario [7,11], one might expect to observe dislocation densities in deformed samples that are equal to or less than the initial dislocation density. Note again that the present measurements should represent lower bounds on the average slip-trace dislocation density. A caveat to these measurements is that the slip-trace density may vary from trace to trace. In addition, it is not possible to stop all tests at the same magnitude of strain, especially for the smaller samples, because of the rapid stochastically occurring strain bursts during testing. As a result, there are variations in the amount of plastic strain imposed from sample to sample. The nominal-strain values are obtained by averaging across the entire gage section of the sample, whereas the local strains at a given slip trace are much larger and vary. Nevertheless, the data shown in Fig. 10 suggest that nominal strain may not be a large variable in the measured dislocation density.

4.3. Sources of increased strength with decreasing sample size

In this section, the measured deformation stresses of the microcrystals are rationalized by combining "traditional" concepts of mean-field forest hardening with relatively new ideas concerning dislocation source operation in small volumes – source truncation hardening [15]. Thus, the average dislocation densities before and after deformation are important inputs into this analysis.

For discussion purposes, some useful nomenclature is proposed that is employed throughout the rest of this document. Given a single-crystal volume of material, there is an inherent "reference stress" associated with the combined effects of the Peierls–Nabarro or lattice-friction stress, initial dislocation-forest density and the stress to activate dislocation sources. In an isotropic pure fcc material at room temperature, the lattice-friction stress is an essentially negligible constant (for stress estimates discussed here, a value of $\tau_o = 2$ MPa was assumed). Therefore, the reference stress is strongly influenced by the initial forest density and source-operation stresses. All subsequent evolution of the dislocation structure must occur under kinetics governed by attaining an "effective stress" that exceeds the sum of the reference-stress components. Therefore, first an evaluation is made of the components of the reference stress and then the effective stress is discussed.

4.3.1. Mean-field forest hardening

Numerous studies since the early 1930s established that dislocation interactions raise the glide resistance of crystals and that a mean-field forest of dislocations gives a theoretical stress component τ_f that is proportional to the scalar density of the forest ρ_f, where

$$\tau_f = k_f Gb \ln\left(\frac{1}{b\sqrt{\rho_f}}\right)\sqrt{\rho_f} \tag{4}$$

b is the burgers vector, G is the shear modulus, and k_f represents the average strength of the dislocation forest [41–50]. The logarithmic term in Eq. (4) accounts for the self interactions of the dislocations bowing at the forest obstacles [51–53]. However, studies have also shown that it is difficult to provide a strictly quantitative value for the magnitude of the hardening coefficient k_f. Thus, for the present study, the experimental findings from Basinski [53] were used to establish quantitatively the mean-field relationship between the forest-hardening stress and the average dislocation forest density.

Basinski showed that, for Cu crystals, the flow stress σ_{flow} scaled with the forest density according to

$$\sigma_{flow} = k\rho_f^{0.425} \tag{5}$$

where the lattice friction stress is negligible, and the scaling coefficient k depends upon G and b. A careful comparison in this study showed that self-consistency between Eqs. (4) and (5) and the experimental data from Basinski is obtained when using a value of $k_f = 0.061$ in Eq. (4).

When practically applying Eq. (4), it is important to recognize that there is some ambiguity associated with selecting the ratio R of the forest density to the total density ($\rho_f = R\rho_t$) for a given test geometry and strain value. As mentioned previously, for most of the present dislocation density measurements, ρ_t was determined. Attempts were made to quantify the density contributions from each of the three active slip systems; however, as a result of imaging difficulties caused by ion damage, accurate measurements were not possible. Such measurements would have

guided selections of the value of *R*. Instead, two values, 1/2 and 3/4, were selected to provide lower and upper bounds to the likely range. The lower bound of 1/2 was taken from Basinski and Basinski [43]. The upper bound value was selected under the assumption that three slip systems of the 12 possible were likely to operate and, those not operating present a dislocation forest to those operating. Note that an examination of the measured ratio ρ_f/ρ_t from the TEM foils described above resulted in values ranging from 0.4 to 1.1, consistent with the ratios selected for analysis.

Using the average nominal measurements for $\rho_o = \rho_f$ ($5.5 \times 10^{12}\,\mathrm{m}^{-2}$ to $1.6 \times 10^{13}\,\mathrm{m}^{-2}$) taken from foils cut parallel to the stress axis, together with Eq. (4), the mean-field forest-hardening stress was assigned a range of values from 14 to 26 MPa.

4.3.2. Source operation and source-truncation hardening

Recently, Parthasarathy et al. [15] proposed a model to describe an average increase in strength of microcrystals considering the combined effects of stochastic variations in dislocation source lengths, a limited sample volume and truncation of sources at the nearby free surfaces. The model is based on the idea that, as sample dimensions are reduced to the same order-of-magnitude as the source lengths, a double-pinned dislocation source becomes a single-pinned source with a free arm interacting with a surface. Source activation is dictated by the operation of the easiest source or the source with the largest source length. Therefore, given a random distribution of sources generated from the initial dislocation density, an average effective source length $\bar{\lambda}$ is related to an effective source stress $\bar{\tau}_s$ through the following relationship:

$$\bar{\tau}_s = k_s G \frac{\ln(\bar{\lambda}/b)}{(\bar{\lambda}/b)} \tag{6}$$

Here, k_s is a source-hardening constant, with magnitude $k_s = 0.12$, derived through a recent study [16].

Using the average ρ_o values taken from the undeformed foils, the strengthening effect associated with source-truncation hardening was derived and is plotted in Fig. 12, together with the initial mean-field forest-hardening stress range, as bands representing the variation in ρ_o measurements.

4.3.3. Mean-field reference stress (MFRS)

Combining the strengthening terms from the lattice-friction stress τ_o, initial forest-hardening stress given by Eq. (4), τ_f and the source-truncation hardening stress given by Eq. (6), $\bar{\tau}_s$, an equation representing the total mean-field reference (MFRS) stress of the microcrystals is established as:

$$\tau_r = \tau_o + k_s G \frac{\ln(\bar{\lambda}/b)}{(\bar{\lambda}/b)} + k_f Gb\,\ln\!\left(\frac{1}{b\sqrt{\rho_t/2}}\right)\sqrt{\rho_t/2} \tag{7}$$

The MFRS is plotted as a function of microcrystal diameter in Fig. 13. Note that, on average, the first and last terms are size independent; thus, the size dependence arises
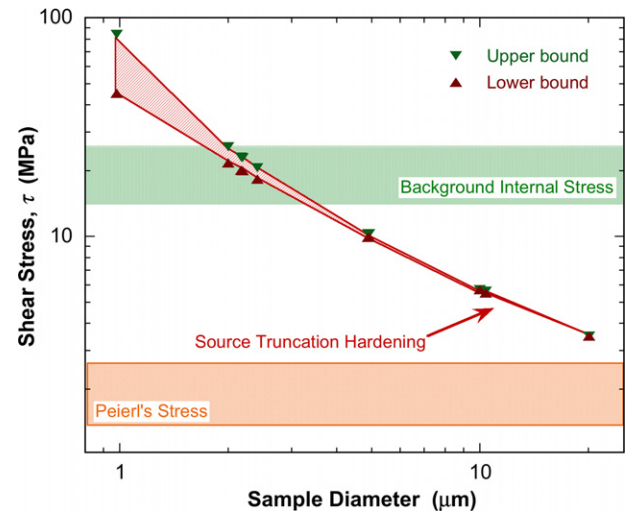
Fig. 12. Using the initial density measurements, the background internal forest-hardening stress and source truncation hardening stresses are plotted as functions of sample diameter.

solely from the source-hardening term when statistical fluctuations of the individual sample initial dislocation densities are neglected. The measured proportional limits (PL) that are compared with the MFRS values in Fig. 13 were determined by isolating the largest linear-elastic slope during the loading of the sample and fitting a line through this array of linear-elastic points. For the smaller samples, this value was typically associated with the first strain-burst event.

It is apparent from Fig. 13 that, for microcrystals larger than ∼5 μm, the observed PL can be satisfactorily explained using the MFRS of Eq. (7). However, for smaller microcrystals, there is a deviation from Eq. (7), suggesting that other hardening mechanisms in the micro-plastic regime lead to an effective stress beyond the MFRS.
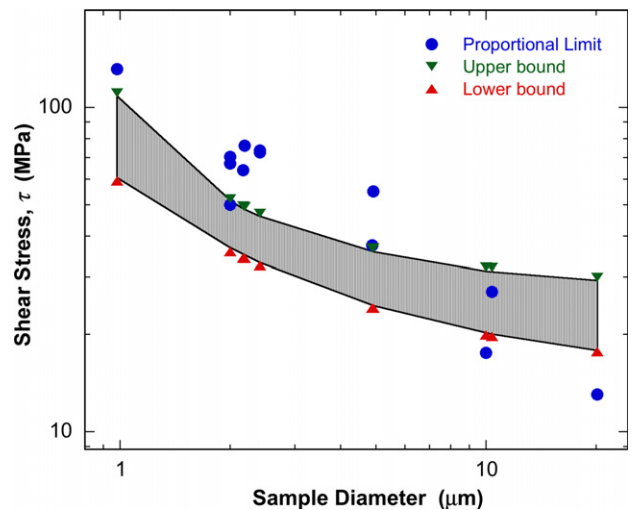
Fig. 13. The proportional limit data from experiment are plotted against the MFRS calculated using Eq. (7) as a function of microsample size.

4.3.4. Shear stress prior to unloading

From the stress–strain curves presented in Fig. 4a, it is clear that there is a transition strain-hardening regime between the PL and the maximum sustainable flow stress, especially for the smallest samples. Less clear is how these samples are able to sustain the very large stresses observed just prior to unloading. Therefore, using the dislocation-density measurements obtained from the sectioned slip planes of deformed microsamples, together with Eq. (4), the values of τ_f associated with these average final densities were determined. In Fig. 14, the combined strengthening effects from all components of the MFRS, with the forest-hardening contribution being corrected for the increase in dislocation density measured at smaller sample sizes, are compared with the observed flow stresses. Note that, as discussed previously, three of the slip systems are active in samples <10 μm in diameter. Thus, it is a possibility that the ratio between the total density and forest density is changing with sample size such that, for larger samples, the R value is closer to 1/2, but may be closer to 3/4 in the smaller samples. This possibility is represented by two sets of calculated values shown in Fig. 14.

The summation of the evolved components of the corrected MFRS also has a size-dependent trend which is very similar to that observed for the flow stress. However, even these combined effects are insufficient to explain the magnitude of the observed flow stresses. This result – in combination with the result of the MFRS being inadequate to account for the observed PL – indicates that there are additional strengthening mechanisms that raise the effective stress at small microcrystal sizes, and these remain active

from the proportional limit throughout the duration of loading.

4.3.5. Specimen-size dependence of the effective stress

Collectively, these results suggest that the dislocation forest itself behaves differently by imposing barriers to dislocation glide that are more effective for microcrystal deformation relative to that for macroscopic crystals. Such a view of an altered forest-hardening response is qualitatively supported by the dislocation percolation areal-glide theory [18], the fundamental thermodynamics of plasticity [54] and recent discrete dislocation simulation studies [17]. Within those frameworks, all samples, macro and micro, have a distribution of slip-plane strengths along the gage length based on the arrangements and type of dislocation lengths present. At smaller sample sizes, the tails of this distribution are truncated, effectively increasing the strength of the weakest slip plane present. Indeed, one should expect that, in the mean-field limit for any crystal at any point in deformation, there exists a correlation length ξ^* for the dislocation ensemble present [18,54], and that ξ^* corresponds to a glide resistance in the mean-field approximation of the forest-hardening theory. For crystals larger than ξ^*, the dislocation ensemble exhibits stress evolution with strain that corresponds to conventional forest-hardening theory. However, when a crystal's characteristic dimensions approach the magnitude of ξ^* or less, the mean-field forest approximation ceases to hold. Then, the heterogeneities of the dislocation ensemble and the size-altered physical attributes of that ensemble lead to a more potent forest-hardening contribution as the weakest elements of the forest are removed from the volume. An accurate theory of such hardening remains to be developed. Sevillano et al. [18] proposed one such definition of ξ^*, but their description was provided within the areal-glide 2D point-pinning model. While that model corresponds well to the multislip Stage II glide processes in large crystals, it does not explicitly consider the evolving dislocation structures of Stage I glide or the expected on-average strengthening of sources expected for microcrystals. For the microcrystal experiments, the slip-trace and slip-band evolution will depend upon the weakest-link statistical events that occur along the length of the sample slip zone (gauge length) for parallel glide planes. Current analyses have not provided a clear view regarding the equivalence of the slip-event correlations among parallel glide planes relative to those occurring for dislocation segments within a glide plane. Thus, further quantitative development of the ξ^*-related size effect on strength is needed.

4.4. Discussion of results in context of existing microcrystal experiments

Looking more broadly at the present results in comparison with related studies and explanations summarized in Section 1, it is important to consider carefully key details for each study. For example, the studies describe different
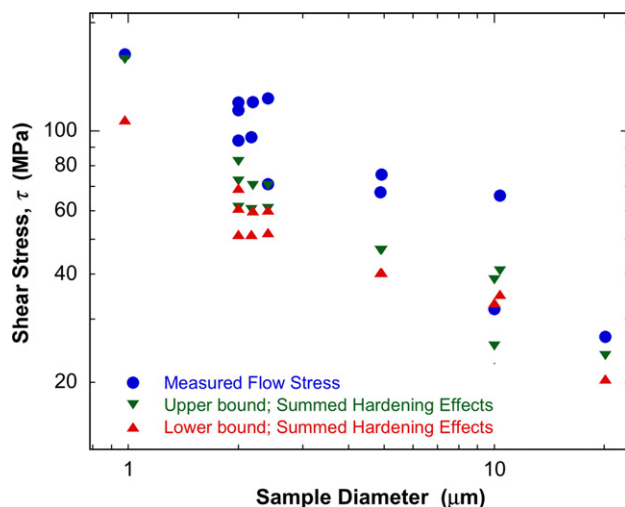

Fig. 14. The combined strengthening effects from the MFRS and forest-hardening, correcting for the increase in dislocation density at smaller sample sizes (from Fig. 9), is compared with the observed flow stresses prior to unloading. The upper and lower bounds result from the variability in R, the correlation factor between the forest and total densities. The error bars associated with the density measurements have been removed for clarity. The combination of all hardening effects explored in this study are insufficient to explain the observed flow stresses.

materials which may behave differently during FIB sample preparation, and which only sparsely overlap in terms of the dimensions of the microcrystals that have been tested. Perhaps more importantly, while the bulk-crystal average dislocation densities are unknown for many of the studies, it is likely that most of the samples tested (i.e. those smaller than ~1 μm) are below the expected strong-obstacle dislocation spacing as estimated in this study. Consequently, the probability that a "starvation-like" concept could apply for those studies is greater. Interestingly, the study by Shan et al. [11] showed that Ni microcrystals as small as ~300 nm can sustain a dislocation structure under stresses as high as 2.6 GPa – a finding that is consistent with source hardening and exhaustion as previously described. Also notable between studies are differences in specimen geometry, testing mode and degree of mechanical constraint during testing. For example, several of the studies are characterized by samples containing significant taper. As discussed by Zhang et al. [21] and Shan et al. [11], the effects of specimen taper are profound. Not only are flow stresses altered, but also values of strain, the SHR and the statistics of sampling the dislocation forest because of the non-uniform stress field. Thus, the exhaustion-hardening regime that is clearly apparent in some studies could well be masked in others. Alternatively, selected studies have been interpreted as supporting the occurrence of strain-gradient induced hardening in the flow response [8–10]. While the present studies offer little insight into those specific results, note again that variations in specimen selection, geometry and preparation technique, degree of mechanical constraint and the form of the flow curves observed during testing all persist as significant differences between results. Further, those studies did not consider possible influences from the mechanisms discussed in Section 4 and in Ref. [15]. Clearly, more directly comparable data are needed to understand these issues fully.

5. Summary and conclusions

Microcrystals often exhibit an early strain, intermittent flow regime that is characterized by a rising effective stress [1,2,4,12]. That stress rise is associated with an effective strain-hardening rate that exceeds the forest-hardening-rate limit associated with Stage II and has been called exhaustion hardening [1]. While the present investigations were insufficient to fully clarify the mechanisms of exhaustion hardening, several important aspects of this regime were identified:

(1) The dislocation substructures formed in these microsamples are on average qualitatively similar to those formed within macroscopic samples experiencing Stage I glide.
(2) The smaller microcrystals (5, 2 and 1 μm) were shown to evolve a lower-bound dislocation density during deformation that is, on average, in excess of their expected average initial density, with an apparent trend that the average density increases with decreasing microcrystal size.
(3) Present evidence indicates that the evolved average slip-trace dislocation density is stored in the early stages of plastic flow and remains nominally constant with strain.
(4) Even the combination of the additional forest-hardening stress expected from the measured slip-trace dislocation densities, taken together with reasonable expectations for the MFRS that include a size-dependent source-hardening contribution, is insufficient to account for the observed flow stress or effective stress.
(5) These results and analyses suggest that microcrystals exhibit a stronger-than-average exhaustion-hardening process when their dimensions are smaller than a correlation length ξ^*, for which the mean-field approximation that is intrinsic to the forest-hardening theory breaks down. The exhaustion-hardening appears to operate via ordinary forest-like dislocation micromechanisms, but with an altered statistical-ensemble response.

References

[1] Dimiduk DM, Uchic MD, Parthasarathy TA. Acta Mater 2005;53:4065.
[2] Greer JR, Oliver WC, Nix WD. Acta Mater 2005;53:1821.
[3] Uchic MD, Dimiduk DM, Florando JN, Nix WD. Mater Res Soc Symp Proc 2003;753:27.
[4] Volkert CA, Lilleodden ET. Philos Mag 2006;86:5567.
[5] Greer JR, Nix WD. Appl Phys A-Mater 2005;A80:1625.
[6] Uchic MD, Dimiduk DM, Florando JN, Nix WD. Science 2004;305:986.
[7] Greer JR, Nix WD. Phys Rev B 2006;73:245410/1.
[8] Maass R, Grolimund D, Van Petegem S, Willimann M, Jensen M, Van Swygenhoven H, et al. Appl Phys Lett 2006;89:151905.
[9] Maass R, Van Petegem S, Van Swygenhoven H, Derlet PM, Volkert CA, Grolimund D. Phys Rev Lett 2007;99:145505.
[10] Maass R, Van Petegem S, Van Swygenhoven H, Uchic MD. Appl Phys Lett 2007;91.
[11] Shan ZW, Mishra R, Syed Asif SA, Warren OL, Minor AM. Nature Mater 2007.
[12] Nadgorny E, Dimiduk DM, Uchic MD. Mater Res Soc Symp Proc 2007:976.
[13] Balint DS, Deshpande VS, Needleman A, Van der Giessen E. Mater Sci Eng 2006;14:409.

[14] Deshpande VS, Needleman A, Van der Giessen E. J Mech Phys Solids 2005;53:2661.

[15] Parthasarathy TA, Rao SI, Dimiduk DM, Uchic MD, Trinkle DR. Scripta Mater 2006;56:313.

[16] Rao SI, Dimiduk DM, Tang M, Parthasarathy TA, Uchic MD, Woodward C. Philos Mag 2007;87:4777.

[17] Rao SI, Dimiduk DM, Tang M, Parthasarathy TA, Uchic MD, Woodward C. DDS Acta Mater 2008; accepted for publication.

[18] Sevillano JG, Arizcorreta IO, Kubin LP. Mater Sci Eng A 2001;309–310:393.

[19] Dimiduk DM, Woodward C, LeSar R, Uchic MD. Science 2006;312:1188.

[20] Uchic MD, Dimiduk DA. Mat Sci Eng A-Struct 2005;400:268.

[21] Zhang H, Schuster BE, Wei Q, Ramesh KT. Scripta Mater 2006;54(2):181.

[22] Choi YS, Uchic MD, Parthasarathy TA, Dimiduk DM. Script Mater 2007;57(9):849.

[23] Raabe D, Ma D, Roters F. Acta Mater 2007;55(13):4567.

[24] Mayer J, Giannuzzi LA, Kamino T, Michael J. MRS Bull 2007;32:400.

[25] Humphreys CJ. Ultramicroscopy 1981;7:7.

[26] Maher DM, Joy DC. Ultramicroscopy 1976;1:239.

[27] Matrin U, Muhle U, Heinrich O. Prakt Metallogr 1995;32.

[28] Delille D, Pantel R, Van Cappellen E. Ultramicroscopy 2001;87:5.

[29] Kelly PM, Jostsons A, Blake RG, Napier JG. Phys Status Solidi A 1975;31:771.

[30] Williams DB, Carter CB. Transmission Electron Microscopy. New York: Plenum Press; 1996.

[31] Stadelmann P. JEMS computer code.

[32] Kruml T, Paidar V, Martin JL. Intermetallics 2000;8:729.

[33] Csikor F, Motz C, Weygand D, Zaiser M, Zapperi S. Science 2007:318.

[34] Miguel M-C, Vespignani A, Zapperi S, Weiss J, Grasso J-R. Nature 2001:410.

[35] Weiss J, Marsan D. Science 2003:299.

[36] Brenner SS. Proc Intern Conf Cooperstown, NY; 1958. p. 157.

[37] Polasik S. MS Thesis. The Ohio State University; 2005.

[38] Mader S. In: Thomas G, Washburn J, editors. Electron microscopy and strength of crystals. New York: Interscience Publishers; 1963. p. 83.

[39] Argon AS. Phys Strength Plast 1969:217.

[40] Norfleet DM. Ph.D. Thesis. Materials science and engineering: The Ohio State University; 2007.

[41] Sevillano JG. In: Mughrabi H, editor. Materials science and technology, vol. 6; 1993. p. 78.

[42] Nabarro F, Basinski ZS, Holt D. Adv Phys 1964;13:193.

[43] Basinski SJ, Basinski ZS. Disloc Solids 1979;4:261.

[44] Pueschl W, Frydman R, Schoeck G. Phys Status Solidi A 1982;74:211.

[45] Schoeck G, Frydman R. Phys Status Solidi B 1972;53:661.

[46] Taylor GI. Theor Proc Roy Soc (London) 1934;A145:362.

[47] Taylor GI. Proc Roy Soc (London) 1934;A145:388.

[48] Orowan E. Z Phys 1934;89:605.

[49] Polanyi M. Z Phys 1934;89:660.

[50] Bailey JE, Hirsch PB. Philos Mag (1798–1977) 1960;5:485.

[51] Madec R, Devincre B, Kubin LP. Phys Rev Lett 2002;89:255508/1.

[52] Bulatov VV, Hsiung LL, Tang M, Arsenlis A, Bartelt MC, Cai W, et al. Nature 2006;440:1174.

[53] Basinski ZS. Scripta Metall 1974;8:1301.

[54] Berdichevsky VL. Scripta Mater 2006;54:711.